



MIT Open Access Articles

Ultrahigh thermal conductivity in isotope-enriched cubic boron nitride

The MIT Faculty has made this article openly available. **Please share** how this access benefits you. Your story matters.

Citation	Chen, Ke et al. "Ultrahigh thermal conductivity in isotope-enriched cubic boron nitride." Science 367, 6477 (January 2020): 555-559 © 2020 The Authors
As Published	http://dx.doi.org/10.1126/science.aaz6149
Publisher	American Association for the Advancement of Science (AAAS)
Version	Author's final manuscript
Citable link	https://hdl.handle.net/1721.1/127819
Terms of Use	Creative Commons Attribution-Noncommercial-Share Alike
Detailed Terms	http://creativecommons.org/licenses/by-nc-sa/4.0/

Ultrahigh thermal conductivity in isotope-enriched cubic boron nitride

Ke Chen^{1*}, Bai Song^{1*†‡}, Navaneetha K. Ravichandran^{2*}, Qiye Zheng^{3§}, Xi Chen^{4#}, Hwijong Lee⁴, Haoran Sun⁵, Sheng Li⁶, Geethal Amila Gamage⁵, Fei Tian⁵, Zhiwei Ding¹, Qichen Song¹, Akash Rai³, Hanlin Wu⁶, Pawan Koirala⁶, Aaron J. Schmidt¹, Kenji Watanabe⁷, Bing Lv⁶, Zhifeng Ren⁵, Li Shi^{4,8}, David G. Cahill³, Takashi Taniguchi⁷, David Broido^{2†}, and Gang Chen^{1†}

¹*Department of Mechanical Engineering, Massachusetts Institute of Technology, Cambridge, MA 02139, USA.*

²*Department of Physics, Boston College, Chestnut Hill, MA 02467, USA.*

³*Department of Materials Science and Engineering and Materials Research Laboratory, University of Illinois at Urbana-Champaign, Urbana, IL 61801, USA.*

⁴*Materials Science and Engineering Program, Texas Materials Institute, The University of Texas at Austin, Austin, TX 78712, USA*

⁵*Department of Physics and Texas Center for Superconductivity, University of Houston, Houston, TX 77204, USA.*

⁶*Department of Physics, The University of Texas at Dallas, Richardson, TX 75080, USA.*

⁷*National Institute for Materials Science, Namiki 1-1, Tsukuba, Ibaraki 305-0044, Japan.*

⁸*Department of Mechanical Engineering, The University of Texas at Austin, Austin, TX 78712, USA.*

[‡]*Current address: Department of Energy and Resources Engineering, and Beijing Innovation Center for Engineering Science and Advanced Technology, Peking University, Beijing 100871, China*

[§]*Current address: Lawrence Berkeley National Laboratory, and Department of Mechanical Engineering, University of California, Berkeley, CA 94720*

[#]*Current address: Department of Electrical and Computer Engineering, University of California, Riverside, CA 92521, USA*

[†]*Corresponding author. Email: songbai@pku.edu.cn (B.S.); broido@bc.edu (D.B.); gchen2@mit.edu (G.C.)*

**These authors contributed equally to this work.*

Abstract:

Materials with high thermal conductivity (κ) are of technological importance and fundamental interest. We grew cubic boron nitride (cBN) crystals with controlled abundance of boron isotopes and measured κ over $1600 \text{ Wm}^{-1}\text{K}^{-1}$ at room temperature in samples with enriched ^{10}B or ^{11}B . In comparison, we found the isotope enhancement of κ is considerably lower for boron phosphide and boron arsenide as the identical isotopic mass disorder becomes increasingly invisible to phonons. The ultrahigh κ in conjunction with its wide bandgap (6.2 eV) makes cBN a promising material for microelectronics thermal management, high-power electronics, and optoelectronics applications.

One Sentence Summary:

A high thermal conductivity was found in isotopically enriched cBN.

Main Text:

Ultrahigh thermal conductivity (κ) materials are desirable for thermal management, and have long been a subject of both fundamental and applied interest (*1*). Despite decades of effort, only a few materials are known to have an ultrahigh thermal conductivity, which we define as exceeding $1000 \text{ Wm}^{-1}\text{K}^{-1}$ at room temperature (RT) (*2*). In metals, free electrons conduct both charge and heat. Therefore, the best electrical conductors like silver and copper also have the highest κ for metals. In semiconductors and insulators, phonons carry the heat. The intricate interplay between lattice dynamics, anharmonicity, and defects dictates thermal transport. Despite the large number of materials that have phonon-dominated heat transport, since 1953 diamond is recognized as the most thermally conductive bulk material at RT (*3*). Besides diamond, a set of non-metallic crystals with high κ was systematically identified by Slack in

1973 (4), including silicon carbide (SiC), boron phosphide (BP), and the cubic, zincblende polymorph of boron nitride (cBN) (5). In addition, Slack (4) proposed guidelines for searching for crystals with high κ , suggesting candidates should be composed of strongly-bonded light element(s) arranged in a simple lattice with low anharmonicity. These guidelines were established via approximate models but captured the essential need for high phonon group velocity and low phonon scattering rates.

Since Slack's work, the κ of diamond ($\sim 2000 \text{ Wm}^{-1}\text{K}^{-1}$ with natural carbon isotopes at RT) (6, 7) has not been surpassed among bulk materials. High thermal conductivities of up to $490 \text{ Wm}^{-1}\text{K}^{-1}$ and $768 \text{ Wm}^{-1}\text{K}^{-1}$ were reported for BP and cBN (8–12), respectively, benefiting from progress in crystal growth and thermal characterization techniques. Unlike cBN and BP, boron arsenide (BAs) has the much heavier arsenic element and was originally estimated to have a κ_{RT} of $200 \text{ Wm}^{-1}\text{K}^{-1}$ (4). In 2013, Lindsay, Broido and Reinecke (13, 14) showed with ab initio simulations that BAs should have a κ_{RT} rivaling that of diamond due to a dramatic reduction in the strength of the lowest-order processes giving intrinsic thermal resistance, three-phonon scattering. Several experiments demonstrated in 2018 a κ_{RT} of $\sim 1200 \text{ Wm}^{-1}\text{K}^{-1}$ (11, 15, 16), making BAs one of the most thermally conductive materials, and consistent with modified predictions that included four-phonon scattering (16, 17).

Apart from the unusual BAs, cBN was predicted to have a κ_{RT} exceeding $2000 \text{ Wm}^{-1}\text{K}^{-1}$ upon isotopic enrichment of the boron atoms using theories that ignored four-phonon scattering (13, 18, 19). We combined experimental characterizations with ab initio simulations that include four-phonon scattering to revisit heat transport in cBN, using synthetic crystals with natural ($^{\text{nat}}\text{B}$) and controlled abundance of boron isotopes. We demonstrated experimentally that $\text{c}^{\text{nat}}\text{BN}$

crystals can have a κ_{RT} over $850 \text{ Wm}^{-1}\text{K}^{-1}$ and enriched $c^{10}\text{B}$ (or ^{11}B) N can reach over $1600 \text{ Wm}^{-1}\text{K}^{-1}$. The ultrahigh κ we measured was consistent with our first-principles calculations, which showed relatively weak effects of higher order anharmonic phonon-phonon interactions on κ in cBN. Furthermore, the $\sim 90\%$ enhancement of κ_{RT} upon boron isotope enrichment qualitatively supported prior calculations (13, 18, 19) and represents a very large RT isotope effect. For isotope-controlled BP and BAs, we only calculated a 31% and a 12% increase in κ_{RT} , which agreed with the small isotope effect we measured. We used simulations to discover the differences between these boron pnictides which can only be understood by considering the subtle interplay between the mutual interactions involving phonons and isotopic disorder.

We prepared four sets of cBN crystals combining natural nitrogen (99.6% ^{14}N and 0.4% ^{15}N) with different boron isotope compositions including $^{\text{nat}}\text{B}$ (21.7% ^{10}B and 78.3% ^{11}B), enriched (99.3%) ^{10}B , enriched (99.2%) ^{11}B , and a roughly equal mix of ^{10}B and ^{11}B ($^{\text{eq}}\text{B}$, 53.1% ^{10}B and 46.9% ^{11}B). The $c^{\text{nat}}\text{BN}$ crystals were obtained by a conventional process using commercial hexagonal boron nitride (hBN, with $^{\text{nat}}\text{B}$) crystals as a starting material (20–22). Because no boron isotope-controlled hBN crystals were commercially available, we grew the other cBN crystals with a metathesis reaction of $\text{Na}^{\text{m}}\text{BH}_4 + \text{NH}_4\text{Cl}$ under high pressure, where $^{\text{m}}\text{B}$ is ^{10}B or ^{11}B (22). By controlling the mixing ratio of $\text{Na}^{10}\text{BH}_4$ and $\text{Na}^{11}\text{BH}_4$, we achieved the desired boron isotope ratios. We obtained nearly colorless $c^{\text{nat}}\text{BN}$ crystals with the conventional process, while the isotope-controlled cBN crystals from the metathesis reaction generally were a light amber color (Fig. 1A and fig. S1). We made single-crystal X-ray diffraction measurements on a $c^{10}\text{BN}$ sample (XRD, Fig. 1B and fig. S1) and found a cubic structure with the $F\bar{4}3m$ space group with a refined lattice constant of $3.6165(5) \text{ \AA}$, in good agreement with literature values (5). Peaks corresponding to different crystallographic directions were observed, indicating the

presence of multiple crystallites (22). We measured the isotope compositions of the cBN crystals using time-of-flight secondary ion mass spectrometry (TOF-SIMS) (Fig. 1C). We also characterized impurities using TOF-SIMS (fig. S2), and found they mainly consisted of carbon and oxygen, consistent with previous results (21). In addition, we used Raman spectroscopy to identify the isotope compositions (Fig. 1D). As the average mass of boron increases from c¹⁰BN to c¹¹BN, the characteristic Raman peaks for the optical phonons at the Brillouin zone-center red-shift noticeably, scaling with the square root of the reciprocal reduced mass and in good agreement with simulations (fig. S27 and Table S1).

We subsequently selected cBN crystals with flat facets of $\sim 200\ \mu\text{m}$ lateral dimension (Fig. 1A) for thermal transport measurements using the laser pump-probe techniques of time- and frequency-domain thermoreflectance (TDTR and FDTR, respectively, Fig. 2, figs. S3-19, and Table S4) (11, 15, 16, 22). The c^{eq}BN crystals yielded the lowest κ_{RT} of $810 \pm 90\ \text{Wm}^{-1}\text{K}^{-1}$ with 53.1% ¹⁰B and 46.9% ¹¹B. A higher κ_{RT} of $880 \pm 90\ \text{Wm}^{-1}\text{K}^{-1}$ was found for the c^{nat}BN crystals with 78.3% ¹¹B, which was also higher than previously reported measurements (Fig. 3C) (11, 12). As we further enriched the ¹¹B isotope to 99.2%, we observed a κ_{RT} of $1660 \pm 170\ \text{Wm}^{-1}\text{K}^{-1}$ in the c¹¹BN crystals. Likewise, we measured an ultrahigh κ_{RT} of $1650 \pm 160\ \text{Wm}^{-1}\text{K}^{-1}$ in the c¹⁰BN crystals with 99.3% ¹⁰B, which we confirmed using a different TDTR platform that gave a κ_{RT} of $1600 \pm 170\ \text{Wm}^{-1}\text{K}^{-1}$ (Fig. 3, inset). We found no substantial effect from the metal transducer layer by using both gold and aluminum (Fig. 2C and Table S4), and no dependence of κ_{RT} on the pump modulation frequency from 2 MHz to 12 MHz (fig. S16) within the experimental uncertainty. We also performed FDTR measurements (Fig. 2B) on the same set of samples to verify the results and obtained κ_{RT} of $800 \pm 50\ \text{Wm}^{-1}\text{K}^{-1}$, $850 \pm 60\ \text{Wm}^{-1}\text{K}^{-1}$, $1620 \pm 100\ \text{Wm}^{-1}\text{K}^{-1}$, and $1580 \pm 100\ \text{Wm}^{-1}\text{K}^{-1}$ for c^{eq}BN, c^{nat}BN, c¹¹BN, and c¹⁰BN, respectively.

We quantify the isotope effect as $P = (\kappa_{\text{enr}} / \kappa_{\text{nat}} - 1) \times 100\%$ where κ_{enr} and κ_{nat} denote the κ of enriched and natural isotope abundances. We observed an unusually high ($P \approx 90\%$) isotope effect on heat transport in cBN at RT, qualitatively consistent with the modeling result of Morelli et al. (18) and a first-principles prediction which included three-phonon and phonon-isotope scattering but ignored four-phonon scattering (13, 19). In comparison, previous experimental efforts only reported a small to moderate isotope effect on other materials. For example, the effect was $P \approx 10\%$ for Si (23), 20% for Ge (24), 5% for GaAs (25), 15% for GaN (26), and 50% for diamond (27). We note that isotope effects of 43% and 58% were measured for hBN (28) and graphene (29), respectively. However, first principles calculations for hBN (28) and graphene (30, 31) found much smaller isotope effects of only around 15%. Furthermore, the smaller theory values for graphene were within the range of the large error bars in experiment (29).

To understand the high thermal conductivity and large isotope effect we observed in cBN, we employed the unified ab initio theory we developed for phonon-mediated thermal transport in solids (22, 32, 33). Briefly, we obtained the required phonon properties and anharmonic interatomic force constants within the density functional theory framework (Quantum ESPRESSO), and acquired the thermal conductivity by solving the Peierls-Boltzmann equation (PBE) for phonon transport including three- and four-phonon scattering, phonon-isotope, and phonon-impurity scattering. Our approach accounts for the distinction between normal and Umklapp scattering, and can accurately predict the thermal and thermodynamic properties of materials from low to high temperatures, from weak to strong anharmonicity, and without any adjustable parameters (22, 32, 33).

We computed the thermal conductivity of ideal cBN crystals versus the percentage of ^{10}B and compared them with the measured values (Fig. 3A). The overall agreement is very good, although some of the measured values for the isotope-enriched cBN samples were noticeably smaller. In order to track down this discrepancy, we computed the influence of carbon and oxygen substitution impurities for boron or nitrogen, and found that the defect of oxygen substituting on the boron site (O_B) can substantially reduce thermal conductivity (22). A realistic O_B concentration around 10^{18} cm^{-3} to 10^{20} cm^{-3} (21) could potentially explain the difference between experiment and theory (gray bars, Fig. 3A), along with the variation across multiple samples and measurements (22). Our simulations predict a high κ for crystals of all boron isotope compositions due to the shared high phonon frequencies and group velocities (figs. S22 and S23). Importantly, a modestly enriched isotope composition such as 98% of either ^{10}B or ^{11}B is sufficient for achieving a κ_RT over $1400 \text{ Wm}^{-1}\text{K}^{-1}$ for cBN. This greatly eases the requirement for boron isotope enrichment, important for facilitating potential applications of isotopically-enriched cBN. Unlike BAs (11, 13–16), the effect of four-phonon scattering is weak for cBN at all boron isotope compositions because three-phonon scattering dominates over the entire frequency range (Fig. 3B).

We theoretically and experimentally determine the isotope effect for κ_RT in BP and BAs, in order to compare with cBN (22). We found reasonable agreement within uncertainty between our measured, calculated κ , and reference κ (9–11, 15, 16) (Fig. 3A, bottom). The κ we measured were $600 \pm 90 \text{ Wm}^{-1}\text{K}^{-1}$, $540 \pm 50 \text{ Wm}^{-1}\text{K}^{-1}$, and $490 \pm 50 \text{ Wm}^{-1}\text{K}^{-1}$ for ^{10}BP (96% ^{10}B), ^{11}BP (96% ^{11}B), and $^\text{nat}\text{BP}$ (19.9% ^{10}B and 80.1% ^{11}B), respectively; and were $1210 \pm 130 \text{ Wm}^{-1}\text{K}^{-1}$, $1180 \pm 130 \text{ Wm}^{-1}\text{K}^{-1}$, and $1240 \pm 130 \text{ Wm}^{-1}\text{K}^{-1}$ for ^{10}BAs (96% ^{10}B), ^{11}BAs (99% ^{11}B), and $^\text{nat}\text{BAs}$ (19.9% ^{10}B and 80.1% ^{11}B), respectively (figs. S20 and S21). The phonon-isotope

scattering had much smaller effects on BP and BAs (Fig. 3A). Quantitatively, the κ_{RT} we computed for cBN, BP, and BAs increased by up to $P = 108\%$, 31% , and 12% , respectively, as the boron isotopes became 100% purified. Such dramatic variation in the isotope effect on these boron pnictides seems puzzling, since boron dictates the isotope disorder in all of them while the pnictogens either have a negligible isotopic impurity (N) or are isotopically pure (P and As). A key difference, however, lies in the pnictogen-to-boron mass ratios which vary from about 1.3 for cBN, to 2.8 for BP, and 6.8 for BAs.

The strong inverse correlation between the isotope effect on κ and the atomic mass ratio is driven largely by the decreasing phonon-isotope scattering rates going from cBN to BP and BAs (Fig. 3B). In all three compounds, heat is carried mainly by acoustic phonons. The large relative mass difference between ^{10}B and ^{11}B contributes to considerable mass fluctuations in $c^{\text{nat}}\text{BN}$, $^{\text{nat}}\text{BP}$, and $^{\text{nat}}\text{BAs}$ (22). With increasing pnictogen-to-boron mass ratio, the vibration amplitudes of the isotopically mixed B atoms decrease sharply for acoustic phonons throughout the Brillouin zone (fig. S25). In BP and BAs, the heavier pnictogens dictate the acoustic phonons while the mass fluctuation on the B sites becomes increasingly invisible, leading to weak phonon-isotope scattering (Fig. 3B). In cBN, the small mass difference between B and N results in large displacements on the B sites for acoustic phonons, which substantially increases the phonon-isotope scattering strength, leading to shorter phonon lifetimes and lower thermal conductivity (Fig. 3B, figs. S25 and S26). The small isotope effect for BAs results not only from the weak phonon-isotope scattering but also from a competition with four-phonon scattering (Fig. 3B). With only three-phonon scattering, a 40% isotope enhancement of κ was calculated for BAs (13), in contrast with the much smaller P of 12% upon including four-phonon scattering.

We studied the temperature dependence of the thermal conductivity of cBN from 250 K to 500 K, which is important for high-power electronics. The thermal conductivities we measured decreased with increasing temperature (Fig. 3C), and agreed well with our *ab initio* calculations for the measured boron isotope compositions except for a small deviation around 250 K. The thermal conductivities of isotope-enriched cBN lie between those of BAs and diamond, with a rate of decrease smaller than BAs but similar to diamond. The more rapid decrease of κ in BAs reflects the important role played by four-phonon scattering. In fact, the κ of $c^{\text{nat}}\text{BN}$ can exceed that of $^{\text{nat}}\text{BAs}$ at elevated temperatures (Fig. 3C and fig. S26), in contrast to previous calculations that did not include four-phonon scattering and found the opposite behavior (13).

We computed the κ accumulation with phonon mean free path (MFP) (34) for cBN at 100 K, 300 K and 500 K (Fig. 3D). Above room temperature, κ saturates beyond a phonon MFP of $\sim 4\ \mu\text{m}$. However, at 100 K, over 35% ($c^{\text{nat}}\text{BN}$) and up to 52% ($c^{10}\text{BN}$) of the thermal conductivity is contributed by phonons with MFP larger than $100\ \mu\text{m}$. Considering the small size of our isotope-engineered samples ($\sim 100\text{--}200\ \mu\text{m}$, Fig. 2B and fig. S1) and the potential existence of multiple crystallites therein (Fig. 1B and fig. S1), we estimated that phonon-boundary scattering could happen at a length scale of $10\ \mu\text{m}$, and therefore substantially limit thermal transport at low temperatures. This may explain the discrepancy between the experiment and calculation at 250 K (Fig. 3C and fig. S28), especially for $c^{10}\text{BN}$ and $c^{11}\text{BN}$ where long-MFP phonons have larger relative contribution to κ and therefore experience a stronger size effect.

Cubic-BN has high hardness, chemical resistance, and is important for machining under conditions where diamond tools may fail (20, 21). Cubic-BN also has a very wide bandgap (6.2 eV), which makes it particularly attractive for ultraviolet optoelectronics (35, 36). We

demonstrated a high thermal conductivity of over $1600 \text{ Wm}^{-1}\text{K}^{-1}$ in isotopically enriched cBN crystals. This ultrahigh thermal conductivity was achieved by removing the strong phonon-isotope scattering that occurs in natural cBN. Ab initio calculations reveal that the strong isotope effect we observed was due to the large relative mass difference in boron isotopes combined with weak three- and four-phonon scattering processes. Our measurements and calculations show that the isotope effect found in cBN was sharply reduced in BP and BAs as the isotopic mass disorder becomes increasingly invisible to the heat-carrying acoustic phonons with increasing pnictogen mass. Our findings demonstrate isotope engineering as one potentially effective method for achieving high thermal conductivity and highlights the potential of isotopically-enriched cBN in critical thermal management applications involving high power, high temperature, and high photon energy.

References and Notes:

1. S. L. Shindé, J. Goela, *High thermal conductivity materials* (Springer, New York, 2006).
2. C. Dames, Ultrahigh thermal conductivity confirmed in boron arsenide. *Science*. **361**, 549–550 (2018).
3. R. Berman, F. E. Simon, J. M. Ziman, The thermal conductivity of diamond at low temperatures. *Proceedings of the Royal Society of London. Series A. Mathematical and Physical Sciences*. **220**, 171–183 (1953).
4. G. A. Slack, Nonmetallic crystals with high thermal conductivity. *Journal of Physics and Chemistry of Solids*. **34**, 321–335 (1973).
5. R. H. Wentorf, Cubic Form of Boron Nitride. *The Journal of Chemical Physics*. **26**, 956–956 (1957).
6. J. R. Olson, R. O. Pohl, J. W. Vandersande, A. Zoltan, T. R. Anthony, W. F. Banholzer, Thermal conductivity of diamond between 170 and 1200 K and the isotope effect. *Phys. Rev. B*. **47**, 14850–14856 (1993).
7. L. Wei, P. K. Kuo, R. L. Thomas, T. R. Anthony, W. F. Banholzer, Thermal conductivity of isotopically modified single crystal diamond. *Phys. Rev. Lett.* **70**, 3764–3767 (1993).

8. Y. Kumashiro, T. Mitsuhashi, S. Okaya, F. Muta, T. Koshiro, Y. Takahashi, M. Mirabayashi, Thermal conductivity of a boron phosphide single-crystal wafer up to high temperature. *Journal of Applied Physics*. **65**, 2147–2148 (1989).
9. J. S. Kang, H. Wu, Y. Hu, Thermal Properties and Phonon Spectral Characterization of Synthetic Boron Phosphide for High Thermal Conductivity Applications. *Nano Lett.* **17**, 7507–7514 (2017).
10. Q. Zheng, S. Li, C. Li, Y. Lv, X. Liu, P. Y. Huang, D. A. Broido, B. Lv, D. G. Cahill, High Thermal Conductivity in Isotopically Enriched Cubic Boron Phosphide. *Advanced Functional Materials*. **28**, 1805116 (2018).
11. J. S. Kang, M. Li, H. Wu, H. Nguyen, Y. Hu, Experimental observation of high thermal conductivity in boron arsenide. *Science*. **361**, 575–578 (2018).
12. N. V. Novikov, T. D. Osetinskaya, A. A. Shul’zhenko, A. P. Podobya, A. N. Sokolov, I. A. Petrusha, Thermal conductivity of single crystals of cubic boron nitride. *Dopov. Akad. Nauk Ukr. RSR, Ser. A: Fiz.-Tekh. Mat. Nauki*, 72–75 (1983).
13. L. Lindsay, D. A. Broido, T. L. Reinecke, First-Principles Determination of Ultrahigh Thermal Conductivity of Boron Arsenide: A Competitor for Diamond? *Phys. Rev. Lett.* **111**, 025901 (2013).
14. D. A. Broido, L. Lindsay, T. L. Reinecke, Ab initio study of the unusual thermal transport properties of boron arsenide and related materials. *Phys. Rev. B*. **88**, 214303 (2013).
15. S. Li, Q. Zheng, Y. Lv, X. Liu, X. Wang, P. Y. Huang, D. G. Cahill, B. Lv, High thermal conductivity in cubic boron arsenide crystals. *Science*. **361**, 579–581 (2018).
16. F. Tian, B. Song, X. Chen, N. K. Ravichandran, Y. Lv, K. Chen, S. Sullivan, J. Kim, Y. Zhou, T.-H. Liu, M. Goni, Z. Ding, J. Sun, G. A. G. U. Gamage, H. Sun, H. Ziyadee, S. Huyan, L. Deng, J. Zhou, A. J. Schmidt, S. Chen, C.-W. Chu, P. Y. Huang, D. Broido, L. Shi, G. Chen, Z. Ren, Unusual high thermal conductivity in boron arsenide bulk crystals. *Science*. **361**, 582–585 (2018).
17. T. Feng, L. Lindsay, X. Ruan, Four-phonon scattering significantly reduces intrinsic thermal conductivity of solids. *Phys. Rev. B*. **96**, 161201 (2017).
18. D. T. Morelli, J. P. Heremans, G. A. Slack, Estimation of the isotope effect on the lattice thermal conductivity of group IV and group III-V semiconductors. *Phys. Rev. B*. **66**, 195304 (2002).
19. L. Lindsay, D. A. Broido, T. L. Reinecke, Phonon-isotope scattering and thermal conductivity in materials with a large isotope effect: A first-principles study. *Phys. Rev. B*. **88**, 144306 (2013).

20. T. Taniguchi, S. Yamaoka, Spontaneous nucleation of cubic boron nitride single crystal by temperature gradient method under high pressure. *Journal of Crystal Growth*. **222**, 549–557 (2001).
21. T. Taniguchi, K. Watanabe, Synthesis of high-purity boron nitride single crystals under high pressure by using Ba–BN solvent. *Journal of Crystal Growth*. **303**, 525–529 (2007).
22. Supplementary materials.
23. A. V. Inyushkin, A. N. Taldenkov, A. M. Gibin, A. V. Gusev, H.-J. Pohl, On the isotope effect in thermal conductivity of silicon. *physica status solidi (c)*. **1**, 2995–2998 (2004).
24. V. I. Ozhogin, A. V. Inyushkin, A. N. Taldenkov, A. V. Tikhomirov, G. É. Popov, E. Haller, K. Itoh, Isotope effect in the thermal conductivity of germanium single crystals. *JETP Lett.* **63**, 490–494 (1996).
25. A. V. Inyushkin, A. N. Taldenkov, A. Y. Yakubovsky, A. V. Markov, L. Moreno-Garsia, B. N. Sharonov, Thermal conductivity of isotopically enriched $^{71}\text{GaAs}$ crystal. *Semicond. Sci. Technol.* **18**, 685–688 (2003).
26. Q. Zheng, C. Li, A. Rai, J. H. Leach, D. A. Broido, D. G. Cahill, Thermal conductivity of GaN, ^{71}GaN , and SiC from 150 K to 850 K. *Phys. Rev. Materials*. **3**, 014601 (2019).
27. T. R. Anthony, W. F. Banholzer, J. F. Fleischer, L. Wei, P. K. Kuo, R. L. Thomas, R. W. Pryor, Thermal diffusivity of isotopically enriched ^{12}C diamond. *Phys. Rev. B*. **42**, 1104–1111 (1990).
28. C. Yuan, J. Li, L. Lindsay, D. Cherns, J. W. Pomeroy, S. Liu, J. H. Edgar, M. Kuball, Modulating the thermal conductivity in hexagonal boron nitride via controlled boron isotope concentration. *Commun Phys*. **2**, 1–8 (2019).
29. S. Chen, Q. Wu, C. Mishra, J. Kang, H. Zhang, K. Cho, W. Cai, A. A. Balandin, R. S. Ruoff, Thermal conductivity of isotopically modified graphene. *Nature Materials*. **11**, 203–207 (2012).
30. G. Fugallo, A. Cepellotti, L. Paulatto, M. Lazzeri, N. Marzari, F. Mauri, Thermal Conductivity of Graphene and Graphite: Collective Excitations and Mean Free Paths. *Nano Lett.* **14**, 6109–6114 (2014).
31. L. Lindsay, W. Li, J. Carrete, N. Mingo, D. A. Broido, T. L. Reinecke, Phonon thermal transport in strained and unstrained graphene from first principles. *Phys. Rev. B*. **89**, 155426 (2014).
32. N. K. Ravichandran, D. Broido, Unified first-principles theory of thermal properties of insulators. *Phys. Rev. B*. **98**, 085205 (2018).
33. N. K. Ravichandran, D. Broido, Non-monotonic pressure dependence of the thermal conductivity of boron arsenide. *Nat Commun*. **10**, 1–8 (2019).

34. C. Dames, G. Chen, in *Thermoelectrics Handbook: Macro to Nano*, D. M. Rowe, Ed. (Taylor and Francis, Boca Raton, 2006), pp. 42–1 to 42–16.
35. K. Watanabe, T. Taniguchi, H. Kanda, Ultraviolet luminescence spectra of boron nitride single crystals grown under high pressure and high temperature. *physica status solidi (a)*. **201**, 2561–2565 (2004).
36. Y. Kubota, K. Watanabe, O. Tsuda, T. Taniguchi, Deep ultraviolet light-emitting hexagonal boron nitride synthesized at atmospheric pressure. *Science*. **317**, 932–934 (2007).
37. H. Chou, A. Ismach, R. Ghosh, R. S. Ruoff, A. Dolocan, Revealing the planar chemistry of two-dimensional heterostructures at the atomic level. *Nature Communications*. **6**, 7482 (2015).
38. A. Schmidt, M. Chiesa, X. Chen, G. Chen, An optical pump-probe technique for measuring the thermal conductivity of liquids. *Review of Scientific Instruments*. **79**, 064902 (2008).
39. A. J. Schmidt, X. Chen, G. Chen, Pulse accumulation, radial heat conduction, and anisotropic thermal conductivity in pump-probe transient thermoreflectance. *Review of Scientific Instruments*. **79**, 114902 (2008).
40. J. Yang, E. Ziade, A. J. Schmidt, Uncertainty analysis of thermoreflectance measurements. *Review of Scientific Instruments*. **87**, 014901 (2016).
41. J. P. Feser, D. G. Cahill, Probing anisotropic heat transport using time-domain thermoreflectance with offset laser spots. *Review of Scientific Instruments*. **83**, 104901 (2012).
42. R. M. Costescu, M. A. Wall, D. G. Cahill, Thermal conductance of epitaxial interfaces. *Phys. Rev. B*. **67**, 054302 (2003).
43. D. G. Cahill, K. Goodson, A. Majumdar, Thermometry and Thermal Transport in Micro/Nanoscale Solid-State Devices and Structures. *J. Heat Transfer*. **124**, 223–241 (2002).
44. D. G. Cahill, Analysis of heat flow in layered structures for time-domain thermoreflectance. *Review of Scientific Instruments*. **75**, 5119–5122 (2004).
45. P. Jiang, X. Qian, R. Yang, Tutorial: Time-domain thermoreflectance (TDTR) for thermal property characterization of bulk and thin film materials. *Journal of Applied Physics*. **124**, 161103 (2018).
46. A. J. Schmidt, R. Cheaito, M. Chiesa, A frequency-domain thermoreflectance method for the characterization of thermal properties. *Review of Scientific Instruments*. **80**, 094901 (2009).
47. S. Tamura, Isotope scattering of large-wave-vector phonons in GaAs and InSb: Deformation-dipole and overlap-shell models. *Phys. Rev. B*. **30**, 849–854 (1984).

48. F. Datchi, A. Dewaele, Y. Le Godec, P. Loubeyre, Equation of state of cubic boron nitride at high pressures and temperatures. *Phys. Rev. B.* **75**, 214104 (2007).
49. C. Stampfl, C. G. Van de Walle, Density-functional calculations for III-V nitrides using the local-density approximation and the generalized gradient approximation. *Phys. Rev. B.* **59**, 5521–5535 (1999).
50. M. Cardona, M. L. W. Thewalt, Isotope effects on the optical spectra of semiconductors. *Rev. Mod. Phys.* **77**, 1173–1224 (2005).

Acknowledgments: We thank Y. Zhou and A. Dolocan for assistance with the thermal and TOF-SIMS measurement, respectively.

Funding: This work was supported by the Office of Naval Research under MURI grant N00014-16-1-2436. Synthesis of the cubic boron nitride crystals was supported by the Elemental Strategy Initiative conducted by the MEXT, Japan and JSPS KAKENHI Grant Numbers 18K19136. The FDTR platform was supported by the National Science Foundation under award no. CBET 1851052. The TOF-SIMS instrument was purchased through the NSF grant DMR-0923096 at Texas Materials Institute, UT Austin.

Author contributions: T.T. and K.W. grew the cBN crystals. H.S., G.A.G., F.T., and Z.R. grew the BAs crystals. S.L., H.W., P. K., and B. L. grew the BP crystals. K.C., B.S., Q.S performed thermal measurements using TDTR and FDTR at MIT. A.J.S. developed the FDTR platform. B.S. wrote the TDTR data analysis code. K.C. and B.S. performed the analysis. Q.Z., A.R., and D.C. performed TDTR measurements at UIUC. B.S. and K.C. measured the Raman spectra, LSCM, and AFM images of cBN. X.C., H.L., and L.S. performed TOF-SIMS and XRD characterizations of cBN. N.K.R. and D.B. performed all the ab initio computations of thermal conductivity. Z.D. calculated the Raman peaks. B.S., K.C., N.K.R., D.B., and G.C. wrote the paper. All authors contributed to the writing of the manuscript. The project was directed and supervised by B.S., D.B., and G.C. **Competing interests:** None. **Data and materials availability:** All data are available in the manuscript and supplementary materials

Supplementary Materials:

Materials and Methods

Figures S1-S30

Tables S1-S4

References

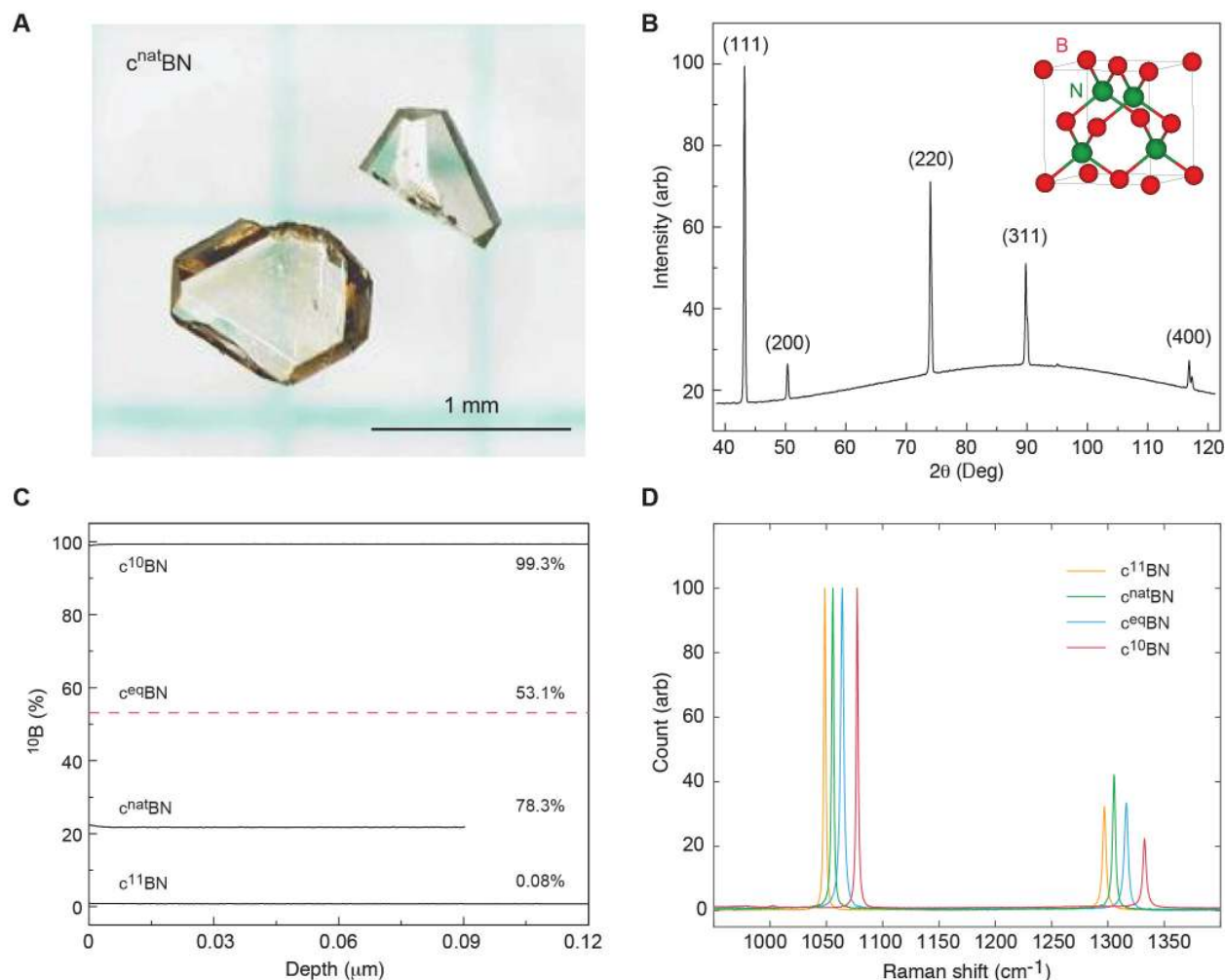


Fig. 1. Structure and composition of homegrown cubic boron nitride crystals. (A) Optical image of two typical $c^{\text{nat}}\text{BN}$ crystals. (B) X-ray diffraction pattern from a $c^{10}\text{BN}$ crystal, indicating a zinc-blende structure (inset) with a lattice constant of $3.6165(5) \text{ \AA}$. Moreover, there appear to be a few crystallites within the sample. Crystals from the same growth batch were used for thermal measurement. (C) Boron isotope concentrations measured by TOF-SIMS. Since no large $c^{\text{eq}}\text{BN}$ crystal was available for an accurate TOF-SIMS measurement, the dashed red line shows an estimation based on the characteristic Raman peaks (fig. S27 and Table S1). (D) Raman peak positions as signatures of boron isotope compositions. Representative **room temperature** spectra normalized to the highest peak for better peak-shift visualization.

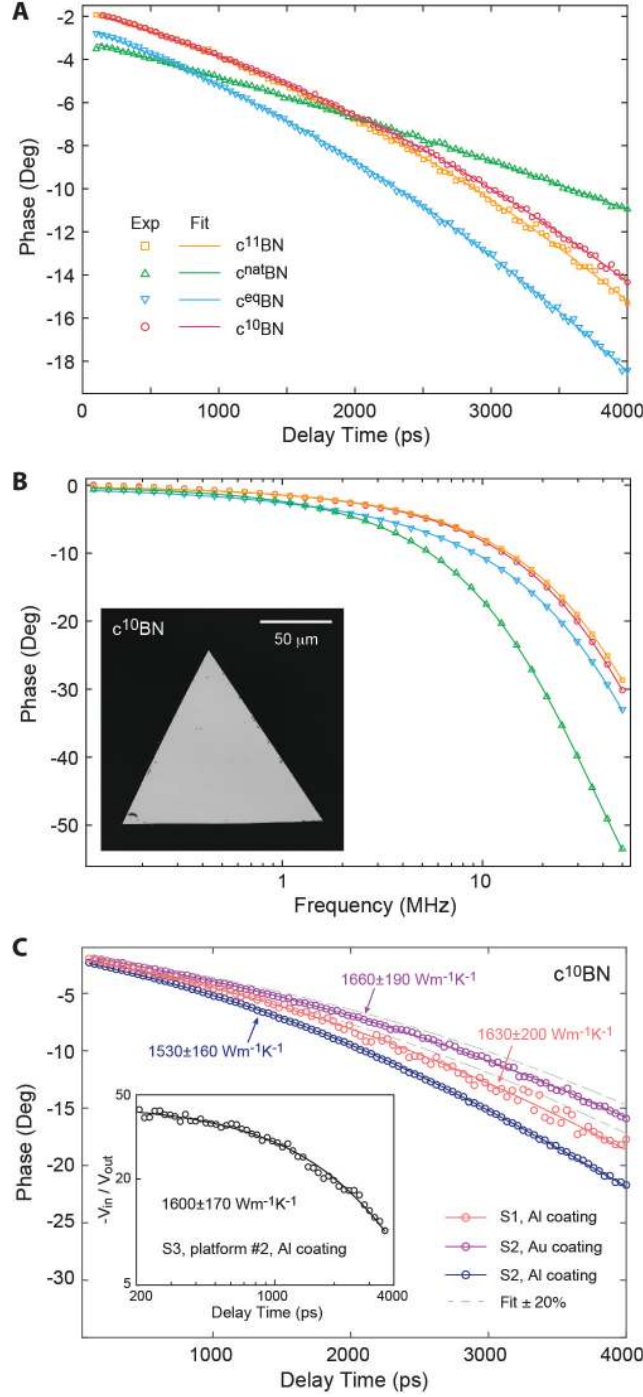


Fig. 2. Heat transport measurement by time- and frequency-domain thermoreflectance. (A) TDTR and **(B)** FDTR phase signals measured at RT at MIT from the same set of cBN crystals together with the fitted curves. The inset of **(B)** shows the flat and clean surface of a $c^{10}\text{BN}$ crystal imaged by laser confocal scanning microscopy (LCSM). **(C)** TDTR signals measured at MIT on two $c^{10}\text{BN}$ crystals and with different metal coatings. The inset shows results for a third $c^{10}\text{BN}$ crystal measured at UIUC on a second TDTR platform with different settings (22).

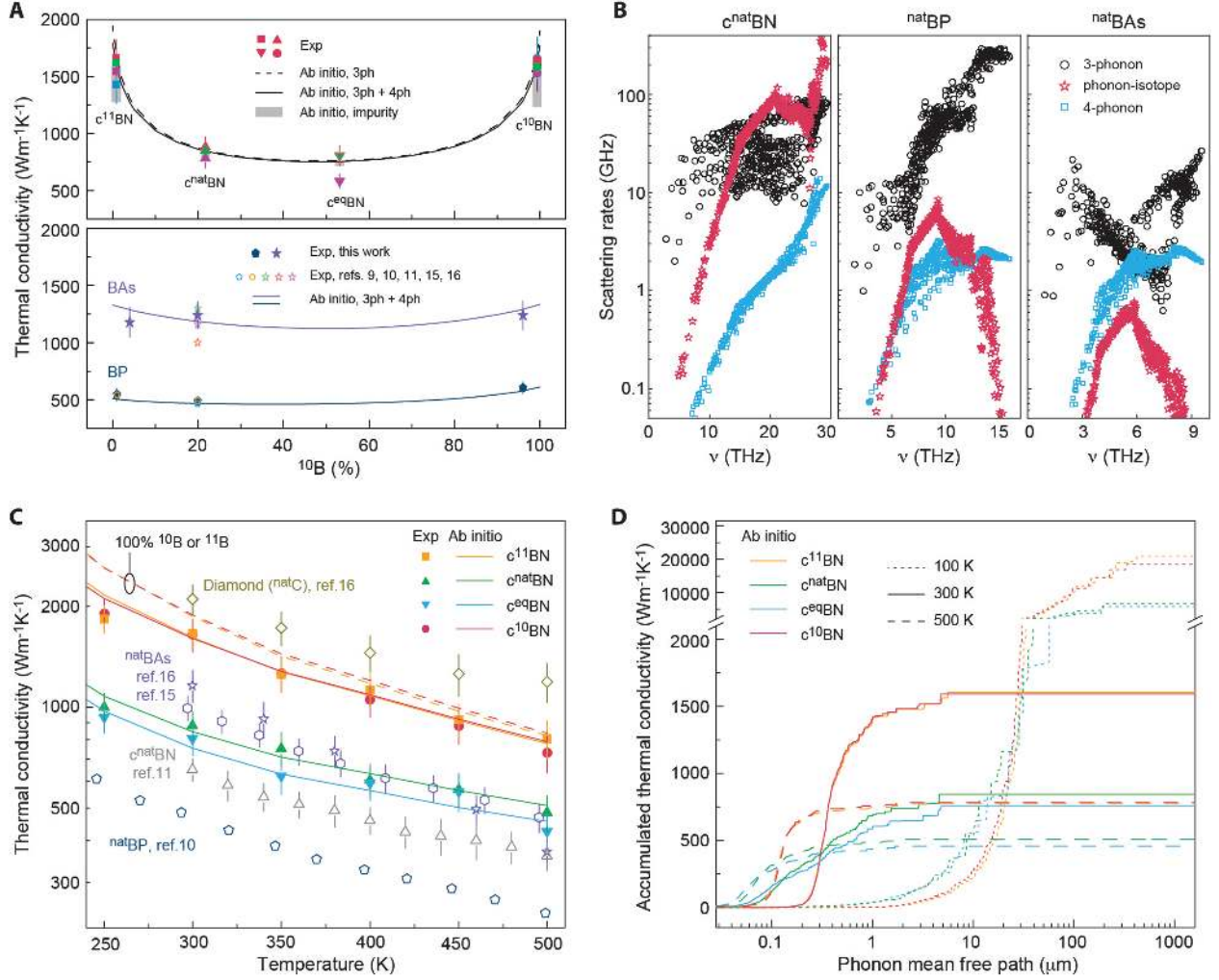


Fig. 3. Isotope effect and temperature dependence of heat transport in cubic boron pnictides. (A) Computed thermal conductivities κ of ideal cBN (top) and BAS and BP (bottom) crystals, compared to measured values as a function of isotope composition. For cBN, the effect of oxygen impurities is indicated by the gray bars. (B) Comparison of various phonon scattering rates in cBN, BP, and BAS with natural B at 300 K obtained from ab initio simulations. Phonon-isotope scattering rates are inversely correlated with the pnictogen-to-boron mass ratio. Four-phonon scattering is weaker than both three-phonon and phonon-isotope scattering in cBN, but exceeds phonon-isotope scattering at all frequencies of interest in BAS. (C) Measured and calculated κ of cBN crystals versus temperature. The solid lines are calculations for the measured B isotope compositions shown in Fig. 1C, while the dashed lines are for 100% ^{10}B or ^{11}B . Literature data for cBN, BP, BAS, and diamond with natural isotopes are also plotted. (D) Calculated κ accumulation with phonon MFP for cBN at 100 K, 300 K, and 500 K.